

The Biconical Outflow in the Seyfert Galaxy NGC 2992

S. Veilleux^{1,2,3}, P. L. Shopbell^{1,3,4}, and S. T. Miller¹

ABSTRACT

We report on a detailed kinematic study of the galactic-scale outflow in the Seyfert galaxy NGC 2992. The TAURUS-2 Imaging Fabry-Perot Interferometer was used on the Anglo-Australian 3.9-m telescope to derive the two-dimensional velocity field of the H α -emitting gas over the central arcminute of NGC 2992. The complete two-dimensional coverage of the data combined with simple kinematic models of rotating axisymmetric disks allows us to differentiate the outflowing material from the line-emitting material associated with the galactic disk. The kinematics of the disk component out to $R = 3.0$ kpc are well modeled by pure circular rotation in a plane inclined at $i = 68^\circ \pm 3^\circ$ from the plane of the sky and with kinematic major axis along P.A. = $32^\circ \pm 3^\circ$. The outflow component is distributed into two wide cones with opening angle $\approx 125 - 135^\circ$ and extending ~ 2.8 kpc ($18''$) on both sides of the nucleus at nearly right angles ($\phi \approx 116^\circ \pm 5^\circ$) to the disk kinematic major axis. The outflow on the SE side of the nucleus is made of two distinct kinematic components interpreted as the front and back walls of a cone. The azimuthal velocity gradient in the back-wall component reflects residual rotational motion which indicates either that the outflowing material was lifted from the disk or that the underlying galactic disk is contributing slightly to this component. A single outflow component is detected in the NW cone. A biconical outflow model with velocities ranging from 50 to 200 km s $^{-1}$ and oriented nearly perpendicular to the galactic disk can explain the data. The broad line profiles and asymmetries in the velocity fields suggest that some of the entrained line-emitting material may lie inside the biconical structure rather than only on the surface of the bicone. The mass involved in this outflow is of order $\sim 1 \times 10^7 n_{e,2}^{-1} M_\odot$, and the bulk and “turbulent” kinematic energies are $\sim 6 \times 10^{53} n_{e,2}^{-1}$ ergs and $\sim 3 \times 10^{54} n_{e,2}^{-1}$ ergs, respectively. The most likely energy source is a hot bipolar thermal wind powered on sub-kpc scale by the AGN and diverted along the galaxy minor axis by the pressure gradient of the ISM in the host galaxy. The data are not consistent with a starburst-driven wind or a collimated outflow powered by radio jets.

¹Department of Astronomy, University of Maryland, College Park, MD 20742; E-mail: veilleux@astro.umd.edu

²Cottrell Scholar of Research Corporation

³Visiting Astronomers, Anglo-Australian Telescope

⁴Current Address: Department of Astronomy, MC 105-24, California Institute of Technology, Pasadena, CA 91125; E-mail: pls@astro.caltech.edu

Subject headings: galaxies: active – galaxies: individual (NGC 2992) – galaxies: jets – galaxies: kinematics and dynamics – galaxies : Seyfert

1. Introduction

Active galactic nuclei (AGN) and nuclear starbursts may severely disrupt the gas phase of galaxies through deposition of a large amount of mechanical energy in the centers of galaxies. As a result, a large-scale galactic wind (“superwind”) that encompasses much of the central regions of these galaxies may be created (e.g., Chevalier & Clegg 1985; Schiano 1985; Tenorio-Tagle & Bodenheimer 1988; Tomisaka & Ikeuchi 1988; MacLow & McCray 1988; MacLow, McCray, & Norman 1989). Depending upon the extent of the halo and its density and upon the wind’s mechanical luminosity and duration, the wind may ultimately blow out through the halo and into the intergalactic medium. The effects of these superwinds may be far-reaching. Bregman (1978) has suggested that the Hubble sequence can be understood in terms of a galaxy’s greater ability to sustain winds with increasing bulge-to-disk ratio. Superwinds may affect the thermal and chemical evolution of galaxies by depositing large quantities of hot, metal-enriched material on the outskirts of galaxies. This widespread circulation of matter and energy between the disks and halos of galaxies may be responsible for the metallicity-radius relation within galaxies and the mass-metallicity relation between galaxies (e.g., Larson & Dinerstein 1975; Vader 1986; Franx & Illingworth 1990; Carollo & Danziger 1994; Zaritsky, Kennicutt, & Huchra 1994; Jablonka, Martin, & Arimoto 1996; Jørgensen, Franx, & Kjaergaard 1996; Pahre, Djorgovski, & de Carvalho 1998; Trager et al. 1998). Superwinds also offer a natural way to create a cosmically evolving population of large, metal-enriched, kinematically-complex gaseous halos, in many ways resembling the sharp metal lines and Lyman-limit systems observed in quasar spectra.

Strong evidence for spatially-resolved starburst-driven winds now exists in several galaxies (e.g., Bland & Tully 1988; Heckman et al. 1990; Lehnert & Heckman 1996; Marlowe et al. 1995; Meurer et al. 1992; Veilleux et al. 1994). The case for spatially resolved outflows in AGN is equally strong (e.g., Cecil, Bland, & Tully 1990; Cecil, Wilson, & Tully 1992; Baum et al. 1993; Wilson et al. 1992; Veilleux, Tully, & Bland-Hawthorn 1993; Colbert et al. 1996a, 1996b, 1998) although here the exact mechanism responsible for the outflow is sometimes uncertain. Possible mechanisms include : (1) thermal wind from a circumnuclear starburst (e.g., Baum et al. 1993), (2) collimated radio jets (e.g., Wilson 1981; Taylor, Dyson, & Axon 1992), and (3) thermal wind produced by the AGN torus (e.g., Krolik & Begelman 1986; Balsara & Krolik 1993) or entrained along the radio ejecta (e.g., Bicknell et al. 1998).

Over the past ten years, our group has been conducting an optical survey of nearby active and starburst galaxies combining Fabry-Perot imaging spectrophotometry with radio and X-ray data to track the energy flow of galactic winds through the various gas phases (see reviews of recent results in Cecil 2000 and Veilleux 2000). The complete spatial and kinematic sampling of the Fabry-Perot data is ideally suited to study the complex and extended morphology of the

warm line-emitting material which is associated with the wind flow. The radio and X-ray data complement the Fabry-Perot data by probing the relativistic and hot gas components, respectively. The high level of sophistication of recent hydrodynamical simulations (e.g., Tomisaka 1990; Slavin & Cox 1992; Mineshige et al. 1993; Suchkov et al. 1994; Strickland & Stevens 2000) has provided the theoretical basis to interpret our data and to predict the evolution and eventual resting place (disk, halo, or intergalactic medium) of the outflowing material. In this paper, we present our results on the Seyfert galaxy NGC 2992.

The proximity of NGC 2992 ($z = 0.0078$ or 31 Mpc assuming $H_0 = 75 \text{ km s}^{-1} \text{ Mpc}^{-1}$; see §4.2 below) provides a spatial scale ($150 \text{ pc arcsec}^{-1}$) which permits a detailed study of the galactic outflow in this galaxy. The AGN host is a Sa galaxy whose high inclination ($i \approx 70^\circ$) is well suited for studies of the extraplanar emission. The galactic disk is rich in HI (Hutchmeier 1982) and CO (Sanders & Mirabel 1985) and is crossed by a disturbed dust lane oriented along P.A. $\approx 30^\circ$. Less than $3'$ to the south-east of NGC 2992 is the companion galaxy NGC 2993. The NGC 2992 – NGC 2993 system (= Arp 245; Arp 1966) is connected by a HI tidal bridge and displays two spectacular tidal tails to the north of NGC 2992 and to the south-east of NGC 2993 (see, e.g., Plate 2 in Ward et al. 1980). The tidal forces associated with this galactic encounter have long been suspected to be the triggering mechanism of the nuclear activity in NGC 2992 (e.g., Burbidge et al. 1972; Osmer, Smith, & Weedman 1974; Ward et al. 1980).

The evidence for AGN activity in NGC 2992 is seen at nearly all wavelengths. The pioneering optical work of Burbidge et al. (1972) and Osmer et al. (1974) revealed a nuclear spectrum dominated by strong high-excitation emission lines. The detection of a broad ($5,500 \text{ km s}^{-1}$) component in the profile of nuclear H α and the identification of NGC 2992 with a strong HEAO-I X-ray source led Ward et al. (1978, 1980) to suggest the presence of a partially obscured AGN in this galaxy. The existence of a broad-line region (BLR) in this object has since been confirmed at optical wavelengths (e.g., Shuder 1980; Véron et al. 1980; Durret & Bergeron 1988) and in the near-infrared (e.g., Rix et al. 1990; Goodrich, Veilleux, & Hill 1994; Veilleux, Goodrich, & Hill 1997). X-ray and HI absorption studies have confirmed the presence of a significant amount of absorbing material in front of the nucleus of NGC 2992 ($N_{\text{H}} \approx 10^{22} \text{ cm}^{-2}$; Gallimore et al. 1999; Weaver et al. 1996 and references therein).

The presence of a galactic-scale outflow in NGC 2992 has been suspected for several years. The 20-cm radio emission from NGC 2992 extends approximately $25''$ (3.75 kpc) along the major axis of the galaxy, but also presents a one-sided $90''$ (13.5 kpc) extension along P.A. $\sim 100^\circ - 130^\circ$, i.e. close to the galaxy minor axis (Ward et al. 1980; Hummel et al. 1983). On smaller scales, a striking “figure-8” structure suggestive of limb-brightened bubbles or magnetic arches is seen at 6 cm extending along P.A. = 160° , about $3''$ ($5''$) north (south) from a weak nuclear source (Ulvestad & Wilson 1984; Wehrle & Morris 1988). The nuclear source has a size $\lesssim 0''.1 - 0''.3$ (15 – 45 pc) and appears to have a flat radio spectrum (Condon et al. 1982; Ulvestad & Wilson 1984; Unger et al. 1986; Sadler et al. 1995). A recent re-analysis of the ROSAT HRI data on NGC 2992 (Colbert et al. 1998) reveals that the soft (0.2 – 2.4 keV) X-ray emission

from this object is extended on a scale of $35 - 45''$ (5.3 – 6.8 kpc) along the galaxy minor axis. The X-ray nebula is therefore roughly cospatial with the large-scale radio emission in this galaxy, suggesting that both are produced by a large-scale galactic outflow. Supporting evidence for a galactic outflow also exists at optical wavelengths. The [O III]-emitting gas is distributed into two conical regions roughly aligned along the galaxy minor axis (e.g., Durret & Bergeron 1987; Werhle & Morris 1988; Allen et al. 1999). Long-slit optical spectroscopy (e.g., Heckman et al. 1981; Colina et al. 1987; Márquez et al. 1998; Allen 1998) indicates that some of the line-emitting gas in NGC 2992 does not follow simple galactic rotation. Near-infrared, extended emission embedded within the northern radio loop was recently detected by Chapman et al. (2000) and deduced to be of non-stellar origin, adding support to the galactic outflow scenario.

However, several fundamental questions remain: What is the geometry of the optical outflow? How is it oriented with respect to the plane of the host galaxy? What are the energetics involved in the outflow? What is powering the outflow? The limited spatial coverage of the long-slit data published so far cannot satisfactorily answer these questions. In this paper, we present the first complete two-dimensional velocity field of the line-emitting gas in NGC 2992. We choose to study the H α emission rather than [O III] to reduce the effects of internal dust extinction (important in this edge-on disk galaxy) and to constrain the kinematics of *both* the galactic disk (bright in H α but faint in [O III]) and the outflowing material. Our paper is organized as follows. In §2, we briefly describe the methods used to obtain and reduce our Fabry-Perot observations. The technique used to decompose the emission-line profiles of NGC 2992 into disk and outflow components is discussed in §3. The results of this analysis are discussed in §4. In that section, we compare our Fabry-Perot data with published radio and X-ray maps, and constrain the three-dimensional kinematics of the outflow and galactic disk. In §5, we discuss the implications of our results on the nature and origin of the galactic wind in this active galaxy. We summarize our results in §6 and discuss future avenues of research.

2. Observations and Data Reduction

The Taurus-2 Fabry-Perot Interferometer (Taylor & Atherton 1980) was used at the f/8 Cassegrain focus of the 3.9-m Anglo-Australian Telescope to obtain in dark and photometric conditions 36 five-minute exposures of redshifted H α in NGC 2992. These data were obtained on 1994 March 10 using the Tek 1024 x 1024 detector (read noise, $\sigma_R = 2.3$ e $^-$, and pixel scale, $0''.594$ px $^{-1}$) under $\sim 1''.5$ seeing. A finesse 50 etalon with free spectral range 57 Å produced a velocity resolution of ~ 50 km s $^{-1}$ (this etalon was borrowed from the HIFI system; Bland & Tully 1989). An order separating filter with a flat-topped transmission profile centered at 6614 Å (55 Å FWHM) passed only one etalon order so the true emission line profile of H α could be synthesized. Exposures were made of diffuse Neon and flat continuum sources to wavelength calibrate and flatfield the images, respectively. Finally, the photometric standard star η Hya was observed through the same setup as the object to provide an absolute flux calibration.

These data were reduced using the methods described in Bland & Tully (1989), Veilleux et al. (1994), and Bland-Hawthorn (1995). The reduction procedure includes flat fielding, spatial registration of the frames, cosmic ray removal, correction for air mass variations, sky continuum and line subtraction, correction for the curvature of the isovelocity surfaces (“phase calibration”), and flux calibration. The velocity calibration was verified using the OH sky line at 6604.13 Å (Osterbrock & Martel 1992).

3. Data Analysis

The data reduction produced a spectral datacube with two spatial and one spectral axes, the latter calibrated in units of wavelength. These data were spectrally smoothed using a 1/4 – 1/2 – 1/4 spectral filter (Hanning smoothing) and then fit with Gaussian emission-line profiles in a semi-autonomous fashion, using software developed by one of us (PLS). No attempt was made to correct for possible underlying Balmer absorption. The profile of this feature is dominated by pressure broadening in the atmospheres of early-type stars, making this feature indistinguishable from a slowly varying continuum over the narrow spectral bandpass of our instrument. For the same reason, the broad H α emission in the nucleus of NGC 2992 was not detected in our data.

As a first coarse attempt, the H α line in each spectrum was fit automatically with a single Gaussian, regardless of the profile’s precise shape. These fits allowed us to develop a rough understanding of both the kinematics and the morphology of the ionized gas emission. The rotation of the galaxy was clearly evident in the velocity structure of these fits, as were regions of radially expanding emission along the galaxy’s minor axis. In terms of morphology, we were able to determine the spatial limits of the emission region, which eventually encompassed some 2,644 spectra. We also identified a narrow region through the center of the galaxy where the prominent dust lane substantially absorbs the H α line emission. This region, including some 845 spectra, was not processed further, as the absorbed line profiles are too complex to allow meaningful Gaussian fits with more than a single velocity component. This region has been noted on Figure 2.

Following these coarse fits, a more detailed series of Gaussian fits were computed, using either one or two distinct velocity components for each spectrum. In certain cases, a third velocity component could perhaps be visually discerned, but the difficulty in constraining the larger number of degrees of freedom in such fits led us to limit ourselves to two components. In many regions, the presence of split (i.e., double) line profiles is very evident, and such regions were manually fit with a pair of Gaussian components, with no constraints on relative velocity or line width. These manual fits were then propagated in an automatic fashion across the emission region. Manual intervention was required where regions of single- and double-component fits merged. In a few instances, the relative line widths of the two components were held constant, to provide more stable convergence of the fits. The result is a collection of 1- and 2-component fits to the H α emission line across the galaxy, where the line velocities and fluxes are relatively smooth functions of spatial position. Examples of fits to the line profiles are shown in Figure 1. The results from

these fits are presented in Figures 2, 4 and 5, and are used in the subsequent analysis.

4. Empirical Results

4.1. Distribution of the Ionized Gas

The distribution of the H α -emitting gas in the disk and outflow components is shown in Figure 2 along with the continuum emission near 6560 Å (rest wavelength). These flux maps were corrected for extinction from our own Galaxy [E(B–V) = 0.060 mag; Burstein & Heiles 1982; Schlegel, Finkbeiner, & Davis 1998] but not for intrinsic reddening (these corrections will be carried out in §5.1). The well-known dust lane is easily visible along P.A. $\approx 30^\circ$ in the continuum image. The total H α flux in these maps amounts to 1.6×10^{-12} erg $^{-1}$ cm $^{-2}$ s $^{-1}$. Our combined H α flux map (Fig. 2b) is very similar to the H α + [N II] $\lambda 6583$ narrow-band images of Wehrle & Morris (1988) and Allen et al. (1999). All of the features seen in their images within $\sim 1'$ of the nucleus are also detected in our H α map. Note the absence of a disk component in the SE quadrant; the emission from the outflowing material in this region overwhelms the emission from the disk (see §§4.2 and 4.3).

The outflow component (Fig. 2d) is distributed into two wide cones which extend up to $\sim 18''$ (2.8 kpc) from the peak in the optical continuum map. Both cones have similar opening angles of order $125^\circ - 135^\circ$. The bisectors of each of the cones coincide with each other and lie along P.A. $\approx 116^\circ$, or almost exactly perpendicular to the kinematic major axis of the inner disk (P.A. $\approx 32^\circ$). This strongly suggests that the axis of the bicone is perpendicular to the galactic disk, and that the material in the SE cone is emerging from under the galaxy disk while the material in the NW cone is emerging from above the disk. If this is the case, the north-west rim of the disk has to be on the near side (see also discussion in Allen et al. 1999).

Figure 3 compares the X-ray (0.2 – 2.4 keV) and radio (6-cm) emission from NGC 2992 with the optical line emission from the outflow component. The RA/DEC coordinates of the Fabry-Perot data were determined by comparing the pixel positions of 5 stars in the field with the corresponding field in the (2nd generation) Digitized Sky Survey. Given the pixel scales of our data and the DSS, as well as the relatively small number of available comparison stars, we estimate the positional accuracy of this method to be $\lesssim 1''$. The absolute positions of the radio maps should be more accurate than this. The X-ray map shown Figure 3 is the ROSAT/HRI image originally published by Weaver et al. (1996) and reanalyzed by Colbert et al. (1998). This image was smoothed with a Gaussian kernel of $\sigma = 24''$ to bring up the faint X-ray bridge which connects NGC 2992 to its companion NGC 2993 and to show the faint extended emission along P.A. $\approx 112^\circ$ (Colbert et al. 1998). This faint extension lies close to the axis of the outflow bicone, suggesting a possible link between the hot and warm gas phases in the outflow. The radio map shown in the upper right panel of Figure 3 is based on the VLA C-configuration data of Colbert et al. (1996a) using 3'' uniform weighting (not shown in the original paper). The high-resolution

radio data (lower right panel in Fig. 3) were taken by Ulvestad & Wilson (1984) using the VLA A-configuration with a spatial resolution $\sim 0''.4$. The SE outflow cone overlaps with the southern portion of the “figure-8” structure seen in the radio. The base of the NW outflow cone lies close to the outer edge of the northern radio “loop”. The position angles of the outflow bisector and the long axis of the “figure-8” structure differ by $\sim 25^\circ - 35^\circ$, but the one-sided 13.5-kpc radio extension detected by Ward et al. (1980) and Hummel et al. (1983) lies roughly along the same direction as the mid-axis of the SE optical cone (P.A. $\sim 100^\circ - 130^\circ$; arrows mark this direction in the right panels of Fig. 3). Interestingly, the high-velocity NW cloud shown in Fig. 4c lies roughly along the major axis of the inner radio structure.

4.2. Velocity Field of the Disk Component

The velocity fields and line width maps of the disk and outflow components are shown in Figures 4 and 5. The uncertainty on these velocities and line widths is $\sim 20 \text{ km s}^{-1}$ in the brighter disk H II regions, but may be 2-3 times larger in the fainter material. The velocity field of the disk component shows the typical “spider diagram” produced by differential rotation. None of the gas in the SE quadrant appears to follow normal galactic rotation; the kinematics of this gas are therefore presented in Figs. 4b and 4c and discussed in the next section. The average line width in the disk component is $\sim 170 \text{ km s}^{-1}$, being significantly larger in the dust lane where selective dust extinction sometimes produces complex profiles (Fig. 5a). In Figure 4a a string of black dots traces the steepest gradient through the observed velocity field (using the method described in Bland 1986); this is the kinematic line of nodes. Figure 6 shows the H α rotation curve along this locus. It rises linearly in the inner region out to a radius of $\sim 1 \text{ kpc}$ where it reaches a local maximum of ~ 190 (NE) – 200 (SW) $\pm 20 \text{ km s}^{-1}$ (or a deprojected value of ~ 205 (NE) – 215 (SW) $\pm 20 \text{ km s}^{-1}$ if $i = 68^\circ$; see below). Beyond this radius, the amplitude of the rotation curve first decreases with increasing radius and then rises again to reach a deprojected velocity amplitude of $\sim 225 \pm 20 \text{ km s}^{-1}$ and perhaps a value even larger at $R \gtrsim 3 \text{ kpc}$. A systemic velocity of $\sim 2335 \pm 20 \text{ km s}^{-1}$ is derived from this rotation curve. This value is confirmed in our more detailed two-dimensional analysis (see below). This value is in good agreement with estimates from other optical datasets [e.g., Nelson & Whittle (1995) and Màrquez et al. (1998) both derived a systemic velocity of 2330 km s^{-1} using stars and the line-emitting gas, respectively; see also Keel 1996], but slightly exceeds the value derived from HI data (e.g., 2314 km s^{-1} from de Vaucouleurs et al. 1991). This apparent discrepancy is probably due to a slight asymmetry between the inner optical rotation curve ($R \lesssim 3 \text{ kpc}$) and the outer H I rotation curve. Tidal forces from the companion galaxy NGC 2993 are likely to disturb the velocity field of the HI material more severely than that of the inner disk.

To better quantify the velocity field of the disk component, we compared our data with simple kinematic models which approximate the intrinsic gas orbits as nonintersecting, inclined elliptical annuli that conserve angular momentum (see Bland 1986 or Staveley-Smith et al. 1990 for a

detailed discussion of these models). We began our analysis by exploring the parameter space for an axisymmetric disk with inclination $60^\circ \leq i \leq 80^\circ$, kinematic major axis $0^\circ \leq \text{P.A.} \leq 45^\circ$, and systemic velocity $2,250 \leq V_{\text{sys}} \leq 2,400 \text{ km s}^{-1}$. This region of parameter space was selected based on the results of previous optical and HI kinematic studies of NGC 2992. We tried to use either (a) a smoothed and symmetric version of the rotation curve shown in Figure 6 or (b) one of Brandt’s (1960) rotation curves. In the first case, the NE and SW sections of the galaxy rotation curve were averaged together and then fit with a fourth-order polynomial. When searching for the best-fitting model, only the inner portion of the disk out to ~ 3 kpc was considered because the velocity field beyond this point is incomplete and possibly affected by the tidal interaction with NGC 2993.

Figure 7a shows the best-fitting axisymmetric model ($i = 68^\circ$, P.A. = 32° , and $V_{\text{sys}} = 2,335 \text{ km s}^{-1}$). The smoothed and symmetric version of the rotation curve was found to give a better fit to the data than the Brandt models. Figure 7b shows the residuals after subtracting the best-fitting model from our measured H α velocity field. The residuals are centered on 0 km s^{-1} with a standard deviation of 32 km s^{-1} . Overall, this axisymmetric model is a good match to the data. We find no evidence for “twisting” of the isovelocity contours in the disk component which would signal the presence of a bar potential. The largest positive residuals between the data and the model are seen $\sim 10'' - 20''$ from the nucleus along P.A. $\approx 40^\circ$. Negative discrepancies are detected in the SW portion of the disk. These discrepancies are due in most part to our use of a symmetric rotation curve in the model; slight asymmetries between the NE and SW sides of the disk are visible in Figures 4a and 6.

Excellent agreement is found between our disk velocity field and the published long-slit data of Màrquez et al. (1998). The model of Màrquez et al. (1998) is similar to our best-fitting disk model: their values of the kinematic major axis (30°), inclination (70°), velocity amplitude (250 km s^{-1}), and systemic velocity ($2,330 \text{ km s}^{-1}$) all lie within the uncertainties of the measurements. However, the two-dimensional coverage of our data allows us to constrain the shape of the rotation curve slightly better, emphasizing in particular the presence of a peak in the velocity curve at ~ 1 kpc on both sides of the nucleus. The velocities of Colina et al. (1987) also agree with ours, although here the comparison is more difficult because their measurements do not extend as far from the nucleus as those of Màrquez et al.

4.3. Velocity Field of the Outflow Component

Two distinct kinematic components are detected in the SE cone (Fig. 4). None of these components shares the kinematics expected from simple galactic rotation (Fig. 7a). One of the components is significantly blueshifted with respect to the expected rotation field of the disk while the other is significantly redshifted. The redshifted component also presents a azimuthal velocity gradient indicative of residual rotational motion, which suggests that the outflowing material was lifted from the disk or that the underlying galactic disk is contributing slightly to this component.

No significant gradient is detected in the blueshifted component. The widths (FWHM) of both components range from 50 km s^{-1} to more than 350 km s^{-1} , with flux-weighted averages of 200 and 150 km s^{-1} for the blueshifted and redshifted components, respectively (Fig. 5).

With the exception of the high-velocity ($170 - 250 \text{ km s}^{-1}$ relative to the systemic velocity) NW cloud, more evident in Figures 4 and 5, the outflow in the NW cone is well modeled by a single emission-line component with FWHM ranging from 75 km s^{-1} to about 350 km s^{-1} (flux-weighted average of 200 km s^{-1}). That is to say most of the substructures detected in the emission-line profiles from the NW quadrant of NGC 2992 are due to the kinematic superposition of the disk and outflow components rather than to the presence of substructure in the outflow itself.

This kinematic asymmetry between the NW and SE outflows is somewhat puzzling. In most wide-angle starburst- and AGN-driven outflows (see results of surveys by Heckman et al. 1990; Lehnert & Heckman 1996; Colbert et al. 1998; Veilleux 2000), double-peaked profiles are detected on both sides of the nucleus, implying that the optical line-emitting gas lies on the surface of expanding bubbles or a biconic structure. The implied velocities in these powerful outflows typically are of order a few hundred km s^{-1} (although exceptions exist: e.g., the outflow velocities in NGC 3079 exceed $1,500 \text{ km s}^{-1}$; Veilleux et al. 1994). The absence of line splitting on one side is sometimes due to obscuration by the disk (e.g., NGC 3079). Can the same thing be happening in NGC 2992? The geometry of the biconical outflow in NGC 2992 (shown in Figure 8) is such that the SE outflow cone is in front of the galaxy disk and the base of the NW outflow is behind it. This may explain the large strength of the SE outflow components relative to the (undetected?) disk component. However, if the gas flows along the walls of the cones, one would expect to detect the blueshifted component of the NW outflow (which is located on the near side of the cone) more easily than the redshifted component; the opposite is seen in NGC 2992. High-resolution HST images of the outflows in M82 (Shopbell et al. 2000) and NGC 3079 (Cecil et al. 2000) indicate that the entrained material is not distributed uniformly on the surface of the bicones (M82) or bubble (NGC 3079), but instead forms a complex network of clouds and filaments where some regions are sometimes devoid of line-emitting material. The near side of the NW cone of NGC 2992 may just be such a region. The absence of warm ($T \approx 10^4 \text{ K}$) line-emitting gas in this region does not preclude the existence of hot or molecular material which would only be detectable in the X-rays or at millimetric wavelengths, respectively.

The biconical outflow model may be constrained further by comparing the velocities of the various kinematic components of the outflow. Using the nomenclature and geometry of Figure 8, we have $|V_{\text{blue}}(\text{SE})| = V_1 \cos \alpha$, $|V_{\text{red}}(\text{NW})| = V_4 \cos \alpha$ and $|V_{\text{red}}(\text{SE})| = V_2 \cos \beta$ where $\alpha = i - \theta/2 \approx 3^\circ$ (assuming $\theta \approx 130^\circ$), $\beta = 180^\circ - \theta - \alpha = 47^\circ$, and V_1 ($= V_4$ if the outflow is bi-symmetric) and V_2 are the outflow velocities at the top and at the base of the bicone, respectively (see Fig. 8). From our data, we measure $|V_{\text{red}}(\text{NW})| = 25 - 220$ (100) km s^{-1} , $|V_{\text{blue}}(\text{SE})| = 15 - 140$ (40) km s^{-1} , and $|V_{\text{red}}(\text{SE})| = 25 - 100$ (40) km s^{-1} , where the values in parentheses are the flux-weighted (\approx mass-weighted) averages. For this calculation, the redshifted velocities in the SE cone were corrected for residual rotational motion by subtracting the expected

disk velocity field (Fig. 7a) from our measured velocities. The results are not consistent with a constant outflow velocity: $V_1 = 25 - 100$ (40) km s $^{-1}$, $V_2 = 40 - 150$ (60) km s $^{-1}$, and $V_4 = 25 - 220$ (100) km s $^{-1}$. Possible trends of decreasing outflow velocities with increasing distance from the nucleus may be present in the V_2 and V_4 components.

Given the complexity of the velocity field in the outflow component, we do not feel that more elaborate modeling of the data is warranted at this stage. Hence, there is no simple way of testing our assumption that the gas flows along the surface of the bicone. However, the large line widths of each of the three main outflow components suggest that the outflow is highly “turbulent” and that each of these components may in fact be the superposition of several filaments at different depths along our line sight. The broad range of velocities and general lack of line splitting in the NW cone may indicate that the line-emitting gas lies inside the biconical structure, filling in some of the velocity space between the front and back walls of the outflow. In this type of mass-loaded outflow, the entrained gas is mixed in with the wind material. In this respect, the NW wind of NGC 2992 may share a strong resemblance with the AGN-driven winds of Circinus (e.g., Veilleux & Bland-Hawthorn 1997; Elmouttie et al. 1998) and NGC 4388 (e.g., Veilleux et al. 1999).

5. Discussion

5.1. Dynamical Timescale, Masses, and Energies

The dynamical time scale of the outflow can be estimated from the linear extent of the outflow and an estimate of the average velocity:

$$t_{\text{dyn}} \approx R/V = 9.8 \times 10^6 \left(R_{\text{obs}}/2 \text{ kpc} \right) \left(V_{\text{obs}}/200 \text{ km s}^{-1} \right)^{-1} \text{ yr} \quad (1)$$

Projection effects may affect this timescale by a factor of ~ 2 .

The ionized mass taking part in the outflow follows from the H α flux. In the following discussion, we parametrize the mass in terms of the density and adopt an electron temperature of 10 4 K (see, e.g., Allen et al. 1999 for measurements of the temperature and density of the ionized material in NGC 2992). The total H α intensity (luminosity) of $\sim 4.3 \times 10^{-13}$ erg s $^{-1}$ cm $^{-2}$ (4.9×10^{40} ergs s $^{-1}$) from the material involved in the outflow yields an ionized mass of $\sim 2 \times 10^6$ n $_{e,2}^{-1}$ M $_{\odot}$, where n $_{e,2}$ is the electron density in units of 100 cm $^{-3}$. In this calculation, we assumed Case B recombination and used an effective recombination coefficient for H α of 8.6×10^{-14} cm $^{-3}$ s $^{-1}$ (Osterbrock 1989). This number has to be corrected for dust obscuration from our Galaxy and intrinsic to NGC 2992. Here, we adopt the average reddening values in the NW and SE cones derived by Allen et al. (1999): $A_V = 0.86$ and 1.8, respectively. Using these values, we get

$$M^{\text{corr}} \approx 1 \times 10^7 n_{e,2}^{-1} \text{ M}_{\odot}. \quad (2)$$

The rate of mass outflow can be estimated if it has been constant over the dynamical age of the

outflow:

$$dM/dt \sim M^{\text{corr}}/t_{\text{dyn}} \approx n_{e,2}^{-1} \text{ M}_\odot \text{ yr}^{-1}. \quad (3)$$

Given the low velocity of the outflow relative to the escape velocity of NGC 2992 ($V_{\text{esc}}(r) > \sqrt{2} V_{\text{rot}}(r) \approx 300 \text{ km s}^{-1}$), the ionized material is likely to be deposited in the halo of the galaxy. This mass outflow rate is a lower limit because it includes only the contribution from the warm ionized H α -emitting material (see §5.2).

To first order, the bulk kinetic energy of the outflowing gas, E_{bulk} , may be derived by summing the bulk kinetic energy over each pixel in the outflow components ($\sum_i 1/2 \delta m_i v_i^2$, where δm_i and v_i are the mass and observed radial velocity at pixel i). Here, we use the rotation-corrected velocity field for the redshifted component in the SE cone while the velocities in the other components are measured with respect to the systemic velocity, 2335 km s^{-1} . We find $E_{\text{bulk}} \approx 2 \times 10^{53} f_{\text{proj}} n_{e,2}^{-1} \text{ ergs}$ where $f_{\text{proj}} \approx 1 - 3$ is the correction factor which accounts for projection effects. The “turbulent” kinematic energy of the outflow component, E_{turb} , may be derived from $\sum_i \delta m_i \sigma_i^2$, where $\sigma_i = \text{FWHM}/1.67$ and FWHM is the full width at half maximum of the line profiles corrected in quadrature for the finite instrumental profile ($\text{FWHM}_i = 50 \text{ km s}^{-1}$); we get $E_{\text{turb}} \approx 7 \times 10^{53} n_{e,2}^{-1} \text{ ergs}$. Applying the reddening corrections of Allen et al. (1999) to each cone, we obtain

$$E_{\text{bulk}}^{\text{corr}} \approx 6 \times 10^{53} f_{\text{proj}} n_{e,2}^{-1} \text{ ergs} \quad (4)$$

and

$$E_{\text{turb}}^{\text{corr}} \approx 3 \times 10^{54} n_{e,2}^{-1} \text{ ergs}. \quad (5)$$

Note that the “turbulent” component of the kinetic energy dominates the outflow in NGC 2992.

Using $n_{e,2} = 1$ as a representative value of the electron density of the outflowing material (Allen et al. 1999) and taking into account projection effects, the total kinetic energy of the outflowing gas is $E_{\text{kin}} = E_{\text{bulk}}^{\text{corr}} + E_{\text{turb}}^{\text{corr}} \approx 4 \times 10^{54} \text{ ergs}$. Using our estimate of the dynamical timescale, we can derive the time-averaged rate of kinetic energy injected into the circumnuclear region:

$$dE_{\text{kin}}/dt \simeq E_{\text{kin}}/t_{\text{dyn}} \approx 10^{40} n_{e,2}^{-1} \text{ erg s}^{-1}. \quad (6)$$

The uncertainty on this number is large (perhaps as much as an order of magnitude) because of unknown projection effects and imperfect reddening correction. Moreover, we must emphasize again that the energetics derived in this section only take into account the optical ionized component of the outflow. Entrainment of the molecular and neutral gas from the disk could significantly increase the energetics of the outflow (e.g., M82: Weiß et al. 1999). The kinetic energy of the ionized outflow in NGC 2992 is comparable to that in the starburst-driven outflow of M82 (Shopbell & Bland-Hawthorn 1998), the AGN-driven outflow of NGC 1068 (Cecil et al. 1990), and even the powerful superwind-blown bubble of NGC 3079 (Veilleux et al. 1994; Cecil et al. 2000). This is somewhat surprising given the relatively small outflow velocities observed in NGC 2992. This is a consequence of the large amount of ionized material entrained in the outflow (eqn. 2) and of the large “turbulent” component to the kinetic energy.

5.2. Origin of the Outflow

In this section, we return to the question of the origin of the outflow in NGC 2992. Three scenarios were mentioned in the Introduction: (1) thermal wind from a circumnuclear starburst, (2) collimated radio jet, and (2) thermal wind produced by the AGN.

5.2.1. Starburst-Driven Wind

This scenario is attractive because it can readily explain the orientation of the outflow along the galaxy minor axis. In this picture, the kinetic energy from strong stellar winds of massive young stars and from type-II supernovae is thermalized, producing a hot, overpressured cavity which bursts out along the minor axis of the galaxy disk entraining with it some of the ambient disk material (e.g., Suchkov et al. 1994, 1996; Strickland & Stevens 2000). A fundamental problem with this scenario is the lack of direct evidence for the presence of a circumnuclear starburst in NGC 2992. The extensive long-slit spectroscopic study by Allen et al. (1999) shows no obvious signs for an on-going nuclear starburst at optical wavelengths (e.g., Wolf-Rayet features). Near-infrared spectroscopy of the nuclear region detects relatively strong H₂ and [Fe II] emission possibly indicative of star formation near the nucleus of NGC 2992, but this emission can also be produced by shocks associated with the nuclear outflow (Goodrich et al. 1994; Veilleux et al. 1997). Substantial amounts of warm dust (*IRAS* 25- μ m-to-60- μ m flux ratio $f_{25}/f_{60} = 0.22$ and far-infrared luminosity $L_{\text{FIR}} = 2.9 \times 10^{10} L_{\odot}$; Spinoglio & Malkan 1989) and neutral and molecular gas are present near the nucleus of NGC 2992 (e.g., Gallimore et al. 1999; Maiolino et al. 1997; Sanders & Mirabel 1985), but there is no evidence that this gas is forming stars at a rate sufficient to sustain the outflow. Finally, there is no sign of a sub-kpc circumnuclear starburst at radio wavelengths. The peculiar “figure-8” radio structure detected on that scale (Ulvestad & Wilson 1984; Wehrle & Morris 1988) is probably of synchrotron origin and is believed to have been produced by the AGN (Wehrle & Morris 1988).

5.2.2. Collimated Radio Jet

The radio morphology is also a problem for the collimated jet-driven outflow model. NGC 2992 does not display the sub-kpc “linear” radio structures seen on arcsecond scale in $\gtrsim 30\%$ of Seyfert galaxies (e.g., Ulvestad & Wilson 1989; Pedlar et al. 1993 and references therein). The resemblance of these linear structures to jet- and lobe-like structures in radio-loud AGNs has been used to argue for the existence of low-power nuclear jets in these Seyfert galaxies (e.g., Kukula et al. 1999 and references therein). The diffuse radio structure of NGC 2992 suggests a more quiescent deposition of energy into the surrounding medium. Equally damaging for the collimated jet model is the large opening angle of the optical outflow and the misalignment between the major axis of the “figure-8” radio structure seen on arcsecond scale and the axis of the optical outflow

(Fig. 3). Radio-optical alignments are often seen in Seyferts with “linear” radio structure (e.g., Whittle et al. 1988; Haniff, Wilson, & Ward 1988) and in powerful radio galaxies (e.g., Chambers, Miley, & van Breugel 1987). Alignment between the optical ionization cones and the nuclear radio source is also frequently seen in Seyfert galaxies (e.g., Wilson & Tsvetanov 1994). The absence of bright radio knots outside of the nucleus of NGC 2992 seems to rule out the possibility that the radio jet has been deflected by a dense cloud in the circumnuclear region (as in NGC 1068; Gallimore, Baum, & O’Dea 1996).

However, the radio data of NGC 2992 do not rule out the possibility that the “figure-8” structure represents radio lobes or bubbles of relativistic plasma (“plasmons”) fed on small ($\lesssim 0''.3 \approx 50$ pc) scale by collimated jets. The linear, supersonic motions of these plasmons may drive bowshocks into the ambient nuclear medium. Several authors have studied the effects of a supersonic light jet or plasmon propagating into the circumnuclear medium of a galaxy (e.g., Pedlar, Dyson, & Unger 1985; Taylor et al. 1989; Taylor, Dyson, & Axon 1992; Ferruit et al. 1997a; Steffen et al. 1997). Using classical equipartition arguments, one finds that the pressure in the relativistic plasma is inadequate to drive high-velocity shocks into the interstellar medium and produce the observed emission line flux. In all these models, the cooled shocked gas is therefore photoionized mainly by the ultraviolet nuclear continuum. These models have had significant success explaining the ENLR of Seyfert galaxies with linear radio structures (e.g., Whittle et al. 1986, 1988; Unger et al. 1987; Taylor et al. 1992; Capetti et al. 1995a,b; Bower, Wilson, & Mulchaey 1994; Bower et al. 1995; Ferruit et al. 1997b; Axon et al. 1998), but to our knowledge it has never been successfully applied to galaxies with diffuse radio morphology like NGC 2992. The lack of spatial correlation between the ridges of radio emission (e.g., the “figure-8” structure) and the optical line-emitting material participating in the outflow in NGC 2992 is difficult to reconcile with the predictions of this model.

5.2.3. Thermal Wind from the AGN

Recently, Bicknell et al. (1998) have argued that the internal energy densities of many Seyfert jets are dominated by thermal plasma rather than relativistic plasma, as it is generally believed to be the case in the more powerful radio galaxies. Focussing on five well-studied Seyferts including NGC 1068, they have shown that an important fraction of the energy and momentum flux originally carried by the radio-emitting jet may be contained in entrained thermal plasma, which is not detected in synchrotron emission. Veilleux et al. (1999) recently argued for a similar mechanism to explain the outflow in NGC 4388 (see also Colbert et al. 1996a, 1998). These “jet-driven” thermal winds are fundamentally different from the “torus-driven” wind of Krolik & Begelman (1986; see also Balsara & Krolik 1993) because the geometry of the former is regulated by that of the radio ejecta rather than by the opening angle of the sub-pc torus. However, these two types of winds may be difficult to differentiate on the kpc scale of the optical outflow in NGC 2992, given the diffuse radio morphology of this object on that scale.

Allen et al. (1999) recently applied this jet-driven wind model to the narrow-line region of NGC 2992 and have argued based on the emission-line ratios that the ENLR in NGC 2992 is powered by shocks with $V_s \approx 300 - 500 \text{ km s}^{-1}$. Our analysis of the galactic outflow now provides additional constraints on this model. As discussed in §4.1, we find the axis of the optical outflow bicone to be roughly aligned with the minor axis of the galaxy and the radio structure on large scale, but to be misaligned by $\sim 44^\circ$ with respect to the major axis of the “figure-8” radio structure on arcsecond scale. As first suggested by Ulvestad & Wilson (1984), this misalignment may be caused by the differential thermal pressure across the radio structure due to static pressure gradients in the interstellar gas (“buoyancy effects”, Henriksen, Vallée, & Bridle 1981; Smith & Norman 1981; Fiedler & Henriksen 1984). The net buoyancy force on the radio ejecta of density ρ_c immersed in a region of density ρ_0 will be $\propto \rho_0 - \rho_c$, and will act to bend the trajectory of the radio plasma away from the major axis of the galaxy as seen in NGC 2992. Note that the large change in direction could not be explained in this fashion for the collimated-jet model (§5.2.2) because only the pressure difference across the jet thickness can contribute to the bending (Fiedler & Henriksen 1984).

A potentially serious problem with the jet-fed thermal wind model is the relatively small outflow velocities detected in NGC 2992 (recall that the flux-weighted average of the apparent outflow velocities is less than 100 km s^{-1} ; §4.3). Shock velocities of $300 - 500 \text{ km s}^{-1}$ are needed to reproduce the line ratios in the ENLR of NGC 2992 (Allen et al. 1999). Although projection effects undoubtedly affect our measurements of the velocities, the corrections are probably not severe [see Fig. 8; the angle α between our line of sight and the near-side (far-side) surface of the SE (NW) cone is only $\sim 3^\circ$ so our viewing angle should allow us to measure most of the actual outflow velocity if the motion is purely radial]. However, one needs to be cautious when comparing shock velocities with gas outflow velocities: the outflow velocities derived from our Fabry-Perot data reflect the motion of the (slow moving) dense entrained material and are almost certainly smaller than the actual shock velocity.

Evidence for high-velocity shocks in NGC 2992 may be found at other wavelengths. Shocks with velocity $V_s \approx 400 \text{ km s}^{-1}$ will heat the ISM to a temperature

$$T_s \approx 2.2 \times 10^6 (V_s/400)^2 \text{ K} \approx 193 (V_s/400)^2 \text{ eV.} \quad (7)$$

This gas may be responsible for some of the extended X-ray emission detected by Colbert et al. (1998). Rough estimates of the pressure of the X-ray emitting gas by Colbert et al. (1998) suggest that it is possibly well above the conventionally calculated non-thermal pressure – this hot gas may therefore be a dynamically important component of the outflow. Given the current estimates of its density (Colbert et al. 1998), the X-ray emitting gas may also be an important contributor to the rate of mass (and metal) outflow in this object (see §5.1). Definite answers to these questions will have to wait until Chandra data on this object become available. These data may also be able to constrain the morphology (jet-like or wide-angled?) of the X-ray gas on sufficiently small scale to help discriminate between the jet-driven wind model of Bicknell et al. (1998) and the torus-driven wind model of Krolik & Begelman (1986) and Balsara & Krolik (1993).

The optical line emission will be produced once the gas cools to $\sim 10^4$ K after

$$t_c \approx 3.2 \times 10^3 n_s^{-1} T_s^{1.5} \simeq 3 \times 10^5 n_s^{-1} (V_s/400)^3 \text{ yr}, \quad (8)$$

where n_s is the postshock density or four times the ambient proton density. The line-emitting gas will be displaced from the shock front by

$$l_c \approx t_c V_s \approx 36 n_0^{-1} (V_s/400)^4 \text{ pc.} \quad (9)$$

Following Dopita & Sutherland (1996), the total energy dissipated in the shock each second is

$$L_{\text{shock}} \simeq \frac{1}{2} \rho A V_s^3 = 7.9 \times 10^{27} n_a A V_s^3 \text{ erg s}^{-1}, \quad (10)$$

where A is the shock surface area in pc^2 , and the $\text{H}\alpha$ luminosities from the shock and the precursor are

$$L(\text{H}\alpha)_{\text{shock}} \approx 3L(\text{H}\beta)_{\text{shock}} = 6.0 \times 10^{33} n_a A (V_s/400)^{2.41} \text{ erg s}^{-1} \quad (11)$$

and

$$L(\text{H}\alpha)_{\text{precursor}} \approx 3L(\text{H}\beta)_{\text{precursor}} = 6.6 \times 10^{33} n_a A (V_s/400)^{2.28} \text{ erg s}^{-1}, \quad (12)$$

respectively. Using an ambient (preshock) ISM density of $\sim 1 \text{ cm}^{-3}$ and $A \simeq 2 \times \pi (1,000)^2 \approx 6 \times 10^6 \text{ pc}^2$ (this is the area at the top of the bicones), we find that the expected $\text{H}\alpha$ luminosity of the shock+precursor model is similar to the dereddened $\text{H}\alpha$ luminosity of the outflow component. Considering the large uncertainties on both the observed and predicted values, it seems physically possible to power a large fraction of the line emission across the bicone with shocks. Allen et al. (1999) came to the same conclusion using line ratio arguments.

6. Conclusions

The complete two-dimensional coverage of our Fabry-Perot data has allowed us to decompose the circumnuclear emission-line region of NGC 2992 into two distinct kinematic components: a rotational component which lies in the plane of the galactic disk and an outflowing component which traces a biconical wind along the minor axis of the galactic disk. Outflow velocities ranging from 50 to 200 km s^{-1} are detected in the biconical region. The presence of two distinct kinematic components in one of the cones suggest that some (but probably not all) of the warm ionized material lies on the surface of the bicone. The mass ($\sim 1 \times 10^7 n_{e,2}^{-1} M_\odot$) and kinematic energy ($\sim 4 \times 10^{54} n_{e,2}^{-1} \text{ ergs}$) involved in this outflow are typical of other starburst- and AGN-driven outflows. Evidence for a slight rotational component in some of the entrained material located in front of the galactic disk suggests that this material has been lifted from the disk or that emission from the underlying disk is contributing to this component. The diffuse radio morphology and absence of direct evidence for a powerful nuclear starburst in this galaxy seem to rule out collimated radio jets or starburst-driven wind as the source of the outflow. By process of elimination, the most

likely scenario is that of a thermally-dominated wind diverted along the galaxy minor axis by the pressure gradient of the ISM and powered on sub-kpc scale by (yet undetected) low-energy radio jets. This picture is consistent with the jet-driven outflow model of Colbert et al. (1996a), Bicknell et al. (1998) and Allen et al. (1999). A similar process was suggested by Veilleux et al. (1999) to explain the outflow in NGC 4388. In NGC 2992, shock velocities of $\sim 400 \text{ km s}^{-1}$ would be sufficient to power the optical line emission from the entrained warm ionized material.

The currently available data on NGC 2992 do not allow us to distinguish between the jet-driven wind of Bicknell et al. (1998) and the torus-driven wind of Krolik & Begelman (1986). Deep radio maps on VLBI scale will be useful to look for the presence of a collimated pc-scale jet. Chandra data of this object would also be helpful to constrain the geometry, temperature and pressure of the X-ray emitting gas and hence the dynamical role of the hot thermal gas in the galactic outflow of NGC 2992. The shock velocities derived from the X-ray data could be directly compared with those necessary to ionize the ENLR clouds.

We thank J. Bland-Hawthorn for help during the observations and analysis and R. B. Tully for the loan of the HIFI etalon and filters. The VLA data used in this analysis were graciously provided to us by A. S. Wilson and E. J. M. Colbert. SV is grateful for partial support of this research by a Cottrell Scholarship awarded by the Research Corporation, NASA/LTSA grant NAG 56547, and NSF/CAREER grant AST-9874973. This research has made use of the NASA/IPAC Extragalactic Database (NED), which is operated by the Jet Propulsion Laboratory, California Institute of Technology, under contract with the National Aeronautics and Space Administration.

REFERENCES

Allen, M. G. 1998, Ph. D. Thesis, Australian National University

Allen, M. G., Dopita, M. A., Tsvetanov, Z. I., & Sutherland, R. S. 1999, *ApJ*, 511, 686

Arp, H. C. 1966, *Atlas of Peculiar Galaxies*

Axon, D. J., Marconi, A., Capetti, A., Macchetto, F. D., Schreier, E., & Robinson, A. 1998, *ApJ*, 496, L75

Balsara, D. S., & Krolik, J. H. 1993, *ApJ*, 402, 109

Baum, S. A., O'Dea, C. P., Dallacassa, D., de Bruyn, A. G., & Pedlar, A. 1993, *ApJ*, 419, 553

Bicknell, G. V., Dopita, M. A., Tsvetanov, Z. I., & Sutherland, R. S. 1998, *ApJ*, 495, 680

Bland J. 1986, Ph.D. thesis, University of Sussex

Bland, J., & Tully, R. B. 1988, *Nature*, 334, 43

Bland, J., & Tully, R. B. 1989, *AJ*, 98, 723

Bland-Hawthorn, J. 1995, in *Trimensional Spectroscopic Methods in Astrophysics*, IAU Coll. 149, ASP Conf. Ser. Vol. 71, eds. G. Comte and M. Marcelin, p. 72

Bower, G., Wilson, A., & Mulchaey, J. 1994, *AJ*, 107, 1686

Bower, G., Wilson, A., Morse, J. A., Gelderman, R., Whittle, M., & Mulchaey, J. 1995, *ApJ*, 454, 106

Brandt, J. C. 1960, *ApJ*, 131, 293

Bregman, J. N. 1978, *ApJ*, 224, 768

Burbidge, E. M., Strittmatter, P. A., Smith, H. E., & Spinrad, H. 1972, *ApJ*, 178, L43

Burstein, D., & Heiles, C. 1982, *AJ*, 87, 1165

Capetti, A., Macchetto, F., Axon, D. J., Sparks, W. B., & Boksenberg, A. 1995a, *ApJ*, 448, 600

Capetti, A., Axon, D. J., Kukula, M., Macchetto, F., Pedlar, A., Sparks, W. B., & Boksenberg, A. 1995b, *ApJ*, 454, L85

Carollo, C. M., & Danziger, I. J. 1994, *MNRAS*, 270, 523

Cecil, G. 2000, *Imaging the Universe in Three Dimensions*, ASP Conf. Ser. Vol. 195, eds. W. van Breugel and J. Bland-Hawthorn, p. 263

Cecil, G., Bland, J., & Tully, R. B. 1990, *ApJ*, 329, 38

Cecil, G., Veilleux, S., Bland-Hawthorn, J., & Filippenko, A. V. 2000, *ApJ*, submitted

Cecil, G., Wilson, A. S., & Tully, R. B. 1992, *ApJ*, 390, 365

Chambers, K. C., Miley, G. K., & van Breugel, W. 1987, *Nature*, 329, 604

Chapman, S. C., Morris, S. L., Alonso-Herrero, A., & Falcke, H. 2000, *MNRAS*, 314, 263

Chevalier, R. A., & Clegg, A. W. 1985, *Nature*, 317, 44

Colbert, E. J. M., Baum, S. A., Gallimore, J. F., O'Dea, C. P., & Christensen, J. A. 1996a, *ApJ*, 467, 551

Colbert, E. J. M., et al. 1996b, *ApJS*, 105, 75

Colbert, E. J. M., Baum, S. A., O'Dea, C. P., & Veilleux, S. 1998, *ApJ*, 496, 786

Colina, L., Fricke, K. J., Kollatschny, W., & Perryman, M. A. C. 1987, *A&A*, 178, 51

Condon, J. J., Condon, M. A., Gisler, G., & Puschell, J. J. 1982, *ApJ*, 252, 102

de Vaucouleurs, G., de Vaucouleurs, A., H. G. Jr. Corwin, Buta, R. J., Paturel, G., & Fouqué, P. 1991, *Third Reference Catalogue of Bright Galaxies* (New York, Springer-Verlag)

Dopita, M. A., & Sutherland, R. S. 1996, *ApJS*, 102, 161

Durret, F. 1990, *A&A*, 229, 351

Durret, F., & Bergeron, J. 1987, *A&A*, 173, 219

Durret, F., & Bergeron, J. 1988, *A&A Suppl.*, 75, 273

Elmouttie, M., Haynes, R. F., Jones, K. L., Sadler, E. M., & Ehle, M. 1998, *MNRAS*, 297, 1202

Ferruit, P., Binette, L., Sutherland, R. S., & Pécontal, E. 1997a, *A&A*, 322, 73

Ferruit, P., Pécontal, E., Wilson, A. S., & Binette, L. 1997b, *A&A*, 328, 493

Fiedler, R., & Henriksen, R. N. 1984, *ApJ*, 281, 554

Franx, M., & Illingworth, G. 1990, *ApJ*, 359, L41

Gallimore, J. F., Baum, S. A., & O'Dea, C. P. 1996, *ApJ*, 464, 198

Gallimore, J. F., Baum, S. A., O'Dea, C. P., Pedlar, A., Brinks, E. 1999, *ApJ*, 524, 684

Goodrich, R. W., Veilleux, S., & Hill, G. J. 1994, *ApJ*, 422, 521

Haniff, C. A., Wilson, A. S., & Ward, M. J. 1988, *ApJ*, 334, 104

Heckman, T. M., Armus, L., & Miley, G. K. 1990, *ApJS*, 74, 833

Heckman, T. M., Miley, G. K., van Breugel, W. J. M., & Butcher, H. R. 1981, *ApJ*, 247, 403

Henriksen, R. N., Vallée, J. P., & Bridle, A. H. 1981, *ApJ*, 249, 40

Hutchmeier, W. K. 1982, *A&A*, 110, 121

Hummel, E., van Gorkom, J. H., & Kotanyi, C. G. 1983, *ApJ*, 267, L5

Jablonka, P., Martin, P., & Arimoto, N. 1996, *AJ*, 112, 1415

Jørgensen, I., Franx, M., & Kjaergaard, P. 1996, *MNRAS*, 280, 167

Keel, W. C. 1996, *ApJS*, 106, 27

Krolik, J. H., & Begelman, M. C. 1986, *ApJ*, 308, L55

Kukula, M. J., Ghosh, T., Pedlar, A., Schilizzi, R. T. 1999, *ApJ*, 518, 117

Larson, R. B., & Dinerstein, H. L. 1975, PASP, 87, 911

Lehnert, M. D., & Heckman, T. M. 1996, ApJ, 462, 651

MacLow, M.-M., & McCray, R. 1988, ApJ, 324, 776

MacLow, M.-M., McCray, R., & Norman, M. L. 1989, ApJ, 337, 141

Maiolino, R., Ruiz, M., Rieke, G. H., & Papadopoulos, P. 1997, ApJ, 485, 552

Marlowe, A. T., Heckman, T. M., Wyse, R. F. G., & Schommer, R. 1995, ApJ, 438, 563

Márquez, I., Boisson, C., Durret, F., & Petitjean, P. 1998, A&A, 333, 459

Meurer, G. R., Freeman, K. C., Dopita, M. A., & Cacciari, C. 1992, AJ, 103, 60

Mineshige, S., Shibata, K., & Shapiro, P. R. 1993, ApJ, 409, 663

Nelson, C. H., & Whittle, M. 1995, ApJS, 99, 67

Osmer, P. S., Smith, M. G., & Weedman, D. W. 1974, ApJ, 192, 279

Osterbrock, D. E. 1989, *Astrophysics of Gaseous Nebulae and Active Galactic Nuclei*, University Science Books

Osterbrock, D. E., & Martel, A. 1992, PASP, 101, 76

Pahre, M. A., Djorgovski, S. G., & de Carvalho, R. R. 1998, AJ, 116, 1591

Pedlar, A., Dyson, J. E., & Unger, S. W. 1985, MNRAS, 214, 463

Pedlar, A., et al. 1993, MNRAS, 263, 471

Rix, H.-W., Carleton, N. P., Rieke, G., & Rieke, M. 1990, ApJ, 363, 480

Sadler, E. M., Slee, O. B., Reynolds, J. E., Roy, A. L. 1995, MNRAS, 276, 1373

Sanders, D. B., & Mirabel, I. F. 1985, ApJ, 298, L31

Schlegel, D. J., Finkbeiner, D. P., & Davis, M. 1998, ApJ, 500, 525

Schiano, A. V. R. 1985, ApJ, 299, 24

Shopbell, P. L., & Bland-Hawthorn, J. 1998, ApJ, 493, 129

Shopbell, P. L., et al. 2000, ApJ, submitted

Shuder, J. M. 1980, ApJ, 240, 32

Slavin, J. D., & Cox, D. P. 1992, ApJ, 392, 131

Smith, M. D., & Norman, C. A. 1981, MNRAS, 194, 771

Spinoglio, L., & Malkan, M. A. 1989, ApJ, 342, 83

Staveley-Smith, L., Bland, J., Axon, D. J., Davies, R. D., & Sharples, R. M. 1990, ApJ, 364, 23

Steffen, W., Gómez, J. L., Williams, R. J. R., Raga, A. C., & Pedlar, A. 1997, MNRAS, 286, 1032

Strickland, D. K., & Stevens, I. R. 2000, MNRAS, 314, 511

Suchkov, A. A., Balsara, D. S., Heckman, T. M., & Leitherer, C. 1994, ApJ, 430, 511

Suchkov, A. A., Berman, V. G., Heckman, T. M., & Balsara, D. S. 1996, *ApJ*, 463, 528

Taylor, K., & Atherton, P. D. 1980, *MNRAS*, 191, 675

Taylor, D., Dyson, J. E., Axon, D. J., & Pedlar, A. 1989, *MNRAS*, 240, 487

Taylor, D., Dyson, J. E., & Axon, D. J. 1992, *MNRAS*, 255, 351

Tenorio-Tagle, G., & Bodenheimer, P. 1988, *ARA&A*, 26, 45

Tomisaka, K. 1990, *ApJ*, 361, L5

Tomisaka, K., & Ikeuchi, S. 1988, *ApJ*, 330, 695

Trager, S. C., Worthey, G., Faber, S. M., Burstein, D., & Gonzalez, J. J. 1998, *ApJS*, 116, 1

Ulvestad, J. S., & Wilson, A. S. 1984, 285, 439

Ulvestad, J. S., & Wilson, A. S. 1989, 343, 659

Unger, S. W., Pedlar, A., Axon, D. J., Whittle, M., Meurs, E. J. A., & Ward, M. 1987, *MNRAS*, 228, 671

Unger, S. W., Pedlar, A., Booler, R. V., Harrison, B. A. 1986, *MNRAS*, 219, 387

Vader, P. 1986, *ApJ*, 305, 669

Veilleux, S. 2000, Imaging the Universe in Three Dimensions, *ASP Conf. Ser.* Vol. 195, eds. W. van Breugel and J. Bland-Hawthorn, p. 277

Veilleux, S., & Bland-Hawthorn, J. 1997, *ApJ*, 479, L105

Veilleux, S., Bland-Hawthorn, J., & Cecil, G. 1999, *ApJ*, 520, 111

Veilleux, S., Cecil, G., Bland-Hawthorn, J., Tully, R. B., Filippenko, A. V., & Sargent, W. L. W. 1994, *ApJ*, 433, 48

Veilleux, S., Goodrich, R. W., & Hill, G. J. 1997, *ApJ*, 477, 631

Veilleux, S., Tully, R. B., & Bland-Hawthorn, J. 1993, *AJ*, 105, 1318

Véron, P., Lindblad, P. O., Zuiderwijk, E. J., Véron, M.-P., & Adam, G. 1980, *A&A*, 87, 245

Ward, M., Penston, M. V., Blades, J. C., & Turtle, A. J. 1980, *MNRAS*, 193, 563

Ward, M., Wilson, A. S., Penston, M. V., Elvis, M., Maccacaro, T., & Tritton, K. P. 1978, *ApJ*, 223, 788

Weaver, K., et al. 1996, *ApJ*, 458, 160

Wehrle, A. E., & Morris, M. 1988, *AJ*, 95, 1689

Weiβ, A., Walter, F., Neininger, N., & Klein, U. 1999, *A&A*, 345, L23

Whittle, M., et al. 1986, *MNRAS*, 222, 189

Whittle, M., Pedlar, A., Meurs, E. J. A., Unger, S. W., Axon, D. J., & Ward, M. J. 1988, *ApJ*, 326, 125

Wilson, A. S. 1981, in Proc. Second ESO/ESA Workshop on Optical Jets in Galaxies, ed. A. F. M. Moorwood & K. Kj  r (Garching: ESO), 125

Wilson, A. S., Elvis, M., Lawrence, A., & Bland-Hawthorn, J. 1992, *ApJ*, 391, L75

Wilson, A. S., & Tsvetanov, Z. 1994, *AJ*, 107, 1227

Zaritsky, D., Kennicutt, R. C. Jr, & Huchra, J. P. 1994, *ApJ*, 420, 87

Fig. 1.— Examples of one- and two-Gaussian fits to the H α emission-line profiles in NGC 2992. The positions relative to the radio nucleus are indicated at the top of each panel, the velocity scale relative to systemic is at the bottom.

Fig. 2.— Distribution of the H α and continuum emission in NGC 2992. (a) Continuum emission at rest wavelength H α , (b) total H α emission, (c) H α emission from the disk component, (d) H α emission from the outflow component. The position of the radio nucleus (“+”) and the extent of the dust lane are indicated on each of these panels. North is at the top and east to the left. Note the absence of a disk component in the east quadrant.

Fig. 3.— Contour maps of the X-ray emission (left panel: ROSAT/HRI data from Colbert et al. 1998) and 6-cm continuum emission (upper right panel: VLA C-configuration data from Colbert et al. 1996a with 3 $''$ uniform weighting; lower right panel: VLA A-configuration data from Ulvestad & Wilson 1984) superimposed on the total H α emission from NGC 2992 (grey-scale). A cross (“+”) in the main figure indicates the position of the radio nucleus. The arrows in the right panels mark the direction of the one-sided 90 $''$ (13.5 kpc) radio extension along P.A. $\sim 100^\circ - 130^\circ$, i.e. close to the axis of the biconical outflow. Same orientation as Fig. 2.

Fig. 4.— (color) Velocity fields of the disk (a) and outflow (b, c) components. The velocity scale is shown at the bottom of the figure. The line of nodes derived from the disk component is shown superposed as a series of black dots in panel a. A cross (“+”) indicates the position of the radio nucleus in each panel. A second, high-velocity redshift component is seen in the SE cone and on the northern tip of the NW cone. Same orientation as Fig. 2.

Fig. 5.— (color) Line widths (FWHM) of the disk (a) and outflow (b, c) components. These widths were corrected in quadrature for the instrumental profile (FWHM $_i = 50$ km s $^{-1}$). The velocity scale is shown at the bottom of the figure. A cross (“+”) indicates the position of the radio nucleus in each panel. Same orientation as Fig. 2.

Fig. 6.— The filled circles show the rotation curve of NGC 2992 derived along the line of nodes (line of steepest gradient) of the disk component. The filled triangles show the velocities along the line of shallowest gradient. The dashed line corresponds to the systemic velocity, 2,335 km s $^{-1}$, derived from model fitting of the 2D velocity field (see Fig. 7). Note the asymmetry between the two sides of the rotation curve.

Fig. 7.— (color) (a) Predicted velocity field for an axisymmetric disk. (b) Residual map (= observed H α velocity field – model). The parameters of the model are described in §4.2. A cross (“+”) indicates the position of the radio nucleus. This simple axisymmetric model fits the data remarkably well. The largest positive and negative residuals between the data and the model are seen $\sim 10'' - 20''$ from the nucleus along P.A. $\approx 40^\circ - 220^\circ$, and are due in the most part to our use of a symmetric rotation curve in the model.

Fig. 8.— Geometry of the idealized biconical outflow. The angles indicated on this figure and derived in the text are $i = 68^\circ$, $\theta = 130^\circ$, $\alpha = 3^\circ$, and $\beta = 47^\circ$. In the simplest form of the model, the gas flows along the surface of the bicone and the outflow velocities are symmetric with respect to the galaxy disk. The Fabry-Perot data do not agree in detail with this simple picture. The line-emitting material appears to partially fill-in the volume of the bicone in NGC 2992 and the kinematic component on the near side of the NW cone is undetected. Asymmetry in the outflow velocities appears to be present in this galaxy: $V_1 = 25 - 100 \text{ km s}^{-1}$, $V_2 = 40 - 150$ and $V_4 = 25 - 220 \text{ km s}^{-1}$. There may also be a trend for decreasing outflow velocities with increasing distance from the nucleus (more evident in the V_2 and V_4 components).

Fig. 1.—

Fig. 2.—

Fig. 3.—

Fig. 4.—

Fig. 5.—

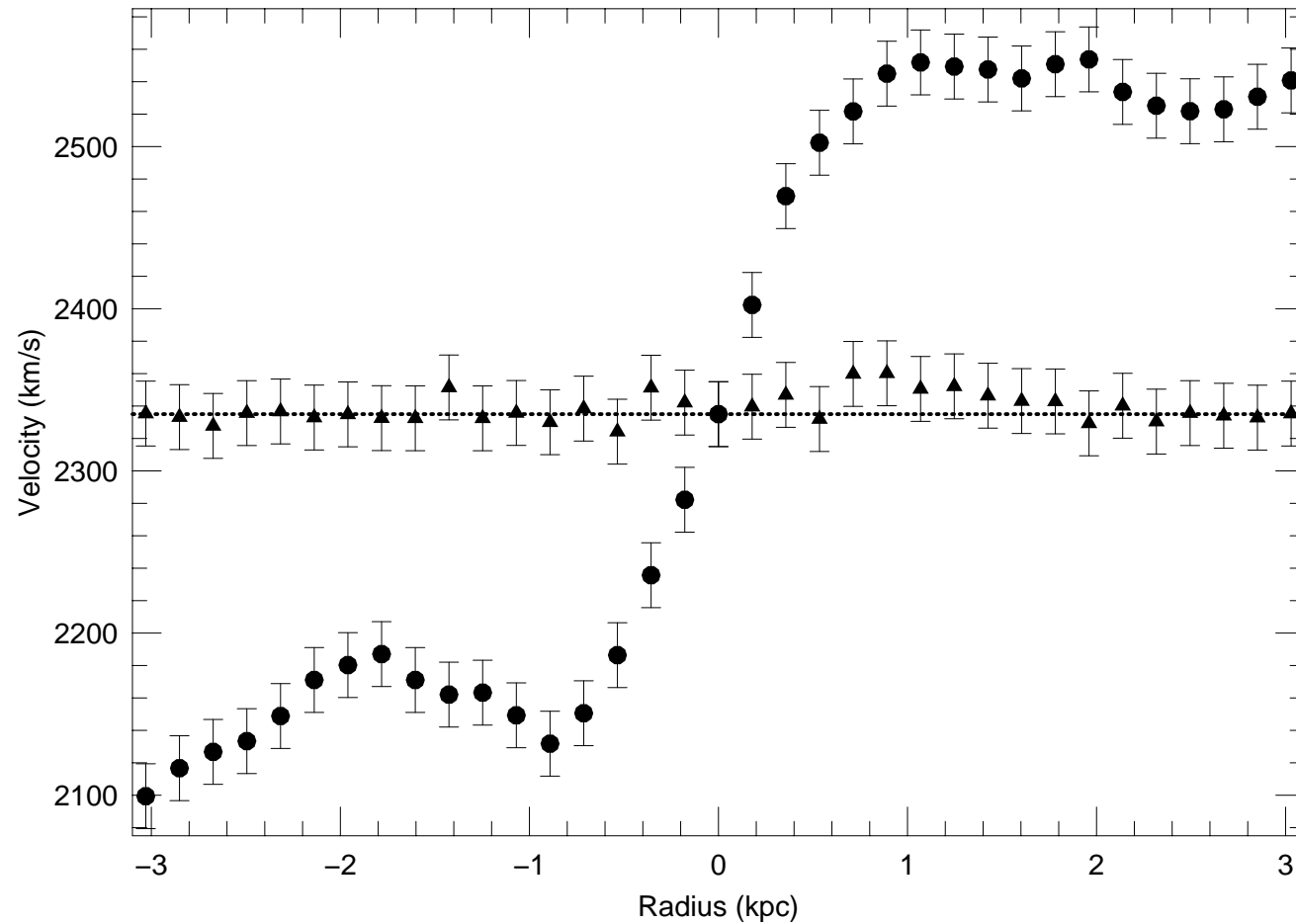
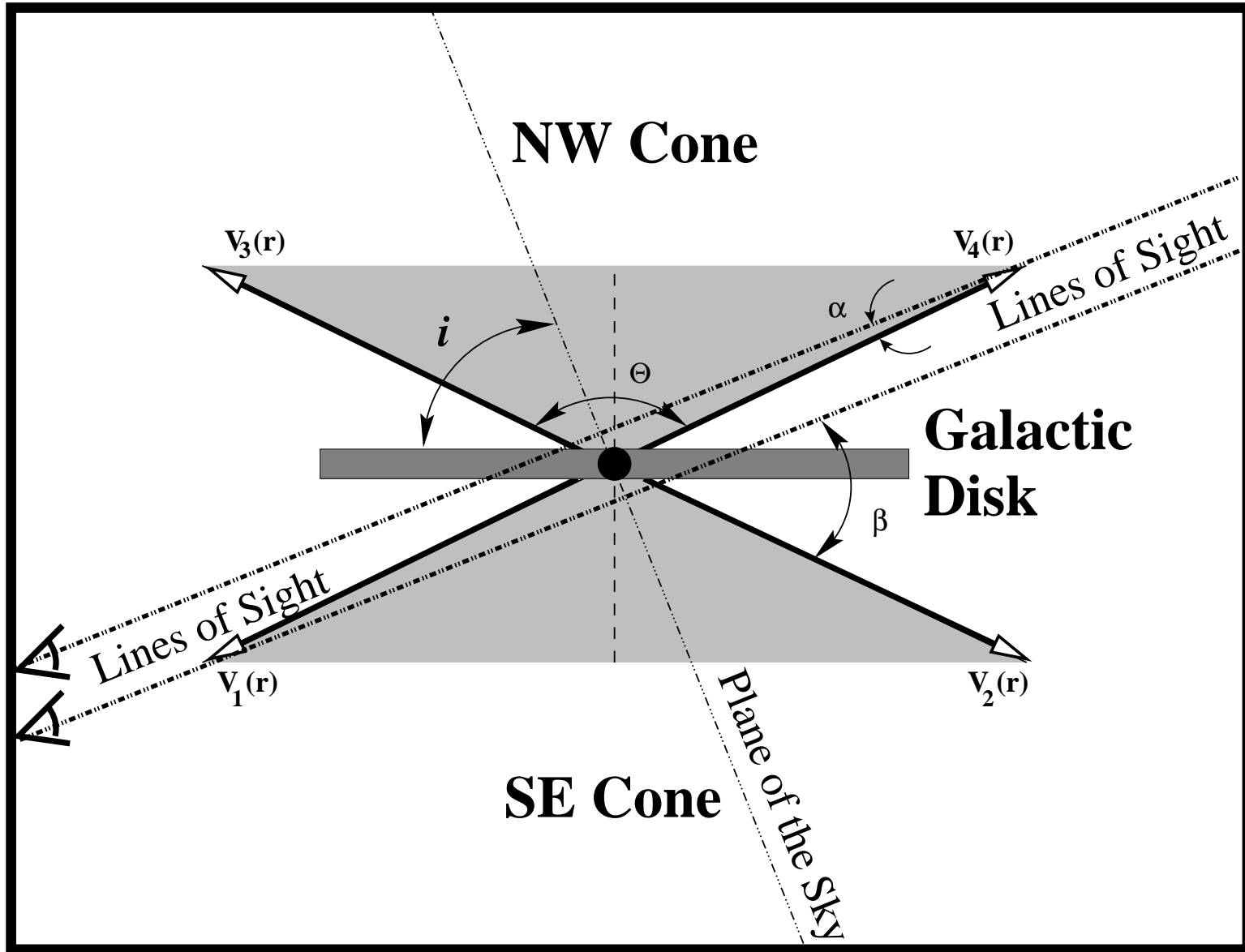


Fig. 7.—



This figure "Veilleux.fig1.jpg" is available in "jpg" format from:

<http://arxiv.org/ps/astro-ph/0010134v1>

This figure "Veilleux.fig2.jpg" is available in "jpg" format from:

<http://arxiv.org/ps/astro-ph/0010134v1>

This figure "Veilleux.fig3.jpg" is available in "jpg" format from:

<http://arxiv.org/ps/astro-ph/0010134v1>

This figure "Veilleux.fig4.jpg" is available in "jpg" format from:

<http://arxiv.org/ps/astro-ph/0010134v1>

This figure "Veilleux.fig5.jpg" is available in "jpg" format from:

<http://arxiv.org/ps/astro-ph/0010134v1>

This figure "Veilleux.fig7.jpg" is available in "jpg" format from:

<http://arxiv.org/ps/astro-ph/0010134v1>